Available online at www.sciencedirect.com
ScienceDirect
Trans. Nonferrous Met. Soc. China 34(2024) 1655−1668
Transactions of Nonferrous Metals Society of China
www.tnmsc.cn

Interaction and initiation mechanism of non-parallel multiple cracks by strain gauge method

Qing-qing SHEN[1,2], Dian-yi HUANG[1], Qiu-hua RAO[1], Wei YI[1], Dong-liang SUN[1], Zhuo LI[1]

1. School of Civil Engineering, Central South University, Changsha 410075, China;
2. College of Civil and Construction Engineering, Hunan Institute of Technology, Hengyang 421002, China

Received 30 December 2022; accepted 8 June 2023

Abstract: The maximum stress intensity factors, $K_{\mathrm{I},k\max}(\theta)$ and $K_{\mathrm{II},k\max}(\theta)$, of three non-parallel oblique cracks were calculated to reveal the interaction mechanism of multiple cracks. The multiple crack initiation criterion was adopted to predict the non-parallel multiple crack initiation parameters. Uniaxial compression tests were performed on rock specimens (red sandstone) with three non-parallel oblique cracks, where the strain near the crack tips was monitored by the strain gauge measurement method to determine the crack initiation sequence. The results showed that the change of crack relative inclination angle had little effect on the fracture trajectory. Multiple crack tips were seldom initiated at the same time. The failure modes of red sandstone specimens with three non-parallel oblique cracks under uniaxial compression are divided into two types: wing crack penetration and wing crack−secondary crack penetration. All of the fracture mechanisms are Mode I (tensile) initiation. The predicted results coincided well with the test results, verifying the validity of the theoretical results.

Key words: non-parallel multiple cracks; interaction mechanism; crack initiation mechanism; strain gauge method

1 Introduction

Fractured rock mass consists of discontinuous cracks with different orientations and relative positions, which have a decisive effect on the deformation and failure patterns of engineered rock masses. Therefore, it is essential to investigate the interaction and fracture mechanisms of rock mass with arbitrary multiple cracks.

Currently, there are mainly two methods of experiment and theory to study multiple crack propagation. In experimental methods, SHEN [1], JIANG et al [2] and GUO et al [3] analyzed the propagation trajectory of rock-like specimens with three types of failure modes. PARK and BOBET [4] revealed the influencing law of the geometric parameters on the strength of gypsum specimens with double non-parallel cracks. LEE and JEON [5], and YANG et al [6] also investigated the crack propagation and coalescence characteristics of rock-like specimens, showing that the coalescence mode of the fractures changed from indirect coalescence to shear coalescence with an increasing ligament angle. In addition, three testing methods are mainly adopted to monitor the propagation process of multiple cracks: the optical method (including caustic line method, photo-elastic method, digital image correlation (DIC) method), acoustic method, and strain gauge electrical method. YANG et al [7] studied the interaction process between the explosion stress wave and the crack propagation through the dynamic photo-elastic method. ZHOU et al [8−11] adopted the acoustic emission (AE) and DIC methods

Corresponding author: Qiu-hua RAO, Tel: +86-731-88876841, E-mail: raoqh@csu.edu.cn;
Wei YI, E-mail: yi.wei@csu.edu.cn
DOI: 10.1016/S1003-6326(24)66497-6

to detect the fracture mode of three parallel cracks under uniaxial compression. As the digital optical method has strict requirements for testing equipment (expensive) and specimens (exposure in the air) and the acoustic method has relatively low precision, these two methods have application limitations. CHAKRABORTY et al [12,13] used the single strain gauge technique to determine the mixed-mode stress intensity factor of an orthotropic laminated plate with double cracks. SARANGI et al [14−16] and LI et al [17] proposed a calculation method for optimum radial strain gauge locations to measure the stress intensity factors using the strain gauge technique.

Since the experimental study lacks quantitative analysis of the fracture mechanism, the theoretical study is necessary for the stress intensity factor (SIF) calculation and the fracture criterion. Presently, there are various analytical solutions for SIF calculation, such as the complex function method [18], energy difference method [19], weight function method [20], stress concentration coefficient method [21], integral transformation method [22], and boundary configuration method [23]. KACHANOV [24] proposed an approximate method to calculate the interacting SIF of the three collinear cracks. CHEN [25] derived two basic solutions for the single crack problem. SHEN et al [26,27] solved the maximum tensile (Mode I) and shear (Mode II) SIFs of the three parallel cracks varying with the relative positions by the pseudo-tension method. There is a lack of SIF calculations and analysis of interaction mechanisms for non-parallel multiple cracks.

The non-parallel initiation of multiple cracks needs to be judged by fracture criteria. There are three classical fracture criteria: (1) stress-based fracture criterion (σ_θ-criterion and $\sigma_{1\theta}$-criterion) [28,29]; (2) strain-based fracture criterion (ε_θ-criterion) [30]; (3) energy-based fracture criterion (G-criterion) [31]; minimum strain energy density criterion (S-criterion) [32]. The above fracture criteria can predict Mode I (tensile) fracture under any loading conditions rather than the true Mode II (shear) fracture of brittle rock where tensile strength is lower than shear strength. A new fracture criteria based on the ratio of the maximum tensile and shear SIF have been proposed by RAO et al [33] to successfully predict both Mode I and Mode II fracture for brittle rock. It has been applied for the single crack under TM (thermo-mechanical) [34], THM (thermo- hydro-mechanical) [35], and THMC (thermo-hydro- mechanical-chemical) [36] coupling conditions and for the multiple parallel cracks under mixed mode conditions. It needs to be further extended for the non-parallel multiple cracks.

In this work, the maximum stress intensity factors, $K_{\mathrm{I},k\max}(\theta)$ and $K_{\mathrm{II},k\max}(\theta)$ of three non-parallel oblique cracks varying with the relative inclination angle were calculated to reveal the interaction mechanism of multiple cracks and determine the strengthening and weakening zones of SIF. The multiple crack initiation criterion based on the ratio of the maximum tension to shear SIF was used to predict the initiation of non-parallel multiple cracks. The strain gauge measurement method was used to test the strain variation law of each crack tip in the red sandstone specimen containing multiple cracks with loading time during the uniaxial compression experiment. The crack initiation sequence at each tip of multiple cracks was determined according to the variation time of the strain gauge displacement. The effect of crack inclination angle on fracture trajectories and stress−strain relationship of multiple cracks was analyzed after uniaxial compression experiments. The failure modes during crack propagation were summarized, and multiple crack propagation mechanisms were revealed.

2 Interaction mechanism for three non-parallel cracks

2.1 Calculation model

Take three equal-length ($2a$=30 mm, where a is the half length of each crack) non-parallel cracks in the infinite plate under uniaxial compression as the analytical model (Fig. 1). The horizontal spacings (along the crack direction) of the center-point connecting lines between the cracks A_2B_2 and A_1B_1, and A_3B_3 and A_1B_1 are D_s and $D_{\mathrm{s}'}$, respectively. The vertical spacing (perpendicular to the crack direction) between the cracks A_2B_2 and A_1B_1, and A_3B_3 and A_1B_1 are D_h and $D_{\mathrm{h}'}$, respectively. Let β denote the inclination angle of crack A_1B_1, and α and γ are the relative inclination angles between A_2B_2 and A_1B_1, and A_3B_3 and A_1B_1, respectively.

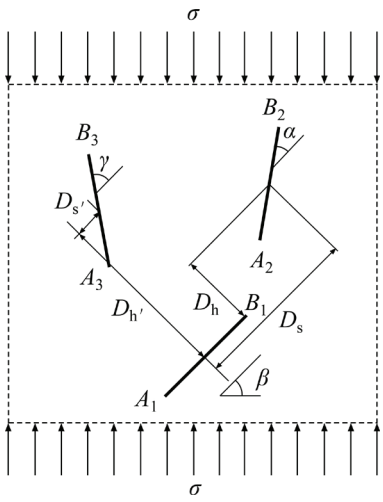

Fig. 1 Schematic diagram of three equal-length non-parallel cracks

The interacting SIFs of each crack (k=1, 2, ⋯, K) on the original crack plane (θ=0°) $K_{\mathrm{I},k}(0)$ and $K_{\mathrm{II},k}(0)$ can be calculated by the following formulas:

$$\begin{cases} K_{\mathrm{I},k}^{\pm}(0)=-\dfrac{1}{\sqrt{\pi a_k}}\displaystyle\int_{-a_k}^{a_k}P_k(s_k)\frac{a_k\pm s_k}{\sqrt{a_k^2-s_k^2}}\mathrm{d}s_k \\ K_{\mathrm{II},k}^{\pm}(0)=-\dfrac{1}{\sqrt{\pi a_k}}\displaystyle\int_{-a_k}^{a_k}Q_k(s_k)\frac{a_k\pm s_k}{\sqrt{a_k^2-s_k^2}}\mathrm{d}s_k \end{cases} \tag{1}$$

where a_k is the half length of the kth crack, s_k is any point on the surface of the kth crack, $P_k(s_k)$ is the normal stress and $Q_k(s_k)$ is the tangential stress existing on the surface of each crack.

The interacting Mode I and Mode II SIFs of the crack in any direction can be determined based on the $K_{\mathrm{I},k}(0)$ and $K_{\mathrm{II},k}(0)$ on its original plane.

$$\begin{cases} K_{\mathrm{I},k}(\theta_k)=K_{\mathrm{I},k}\cos^3\dfrac{\theta_k}{2}-3K_{\mathrm{II},k}\sin\dfrac{\theta_k}{2}\cos^2\dfrac{\theta_k}{2} \\ K_{\mathrm{II},k}(\theta_k)=K_{\mathrm{I},k}\sin\dfrac{\theta_k}{2}\cos^2\dfrac{\theta}{2}+ \\ \quad K_{\mathrm{II},k}\cos\dfrac{\theta_k}{2}(1-3\sin^2\dfrac{\theta_k}{2}) \end{cases} \tag{2}$$

where θ_k is the arbitrary crack plane, $0°\le\theta_k\le360°$.

$K_{\mathrm{I},k\max}(\theta)$ and $K_{\mathrm{II},k\max}(\theta)$ (the maximum values of $K_{\mathrm{I},k}(0)$ and $K_{\mathrm{II},k}(0)$ at θ_{IC} and θ_{IIC}, respectively) can be determined by the following equations:

$$\begin{cases} \dfrac{\partial K_{\mathrm{I},k}(\theta_k)}{\partial\theta}=0,\ \dfrac{\partial^2K_{\mathrm{I},k}(\theta_k)}{\partial\theta^2}<0 \\ \dfrac{\partial K_{\mathrm{II},k}(\theta_k)}{\partial\theta}=0,\ \dfrac{\partial^2K_{\mathrm{II},k}(\theta_k)}{\partial\theta^2}<0 \end{cases} \tag{3}$$

2.2 Influence of relative inclination angles on interacting SIF

(1) Variation of α

Let D_{s}=D_{s}=0, D_{h}=20 mm, D_{h}=40 mm, β=45°, γ=0°, a=15 mm, with only a change of α. For multiple cracks, defining $K_{\mathrm{I},k\max}(\theta)/K^0_{\mathrm{I},\max}(\theta)$<1 (or $K_{\mathrm{II},k\max}(\theta)/K^0_{\mathrm{II},\max}(\theta)$<1) as the weakening-interaction and $K_{\mathrm{I},k\max}(\theta)/K^0_{\mathrm{I},\max}(\theta)$>1 (or $K_{\mathrm{II},k\max}(\theta)/K^0_{\mathrm{II},\max}(\theta)$<1) as the strengthening-interaction, and $K_{\mathrm{I},k\max}(\theta)/K^0_{\mathrm{I},\max}(\theta)$=1 (or $K_{\mathrm{II},k\max}(\theta)/K^0_{\mathrm{II},\max}(\theta)$=1) as the non-interaction, $K^0_{\mathrm{I},\max}(\theta)$ and $K^0_{\mathrm{II},\max}(\theta)$ are the maximum Mode I and Mode II SIFs of the single crack with the same length ($2a$=30 mm) and inclination angle (β=45°).

Figure 2 indicates the influence of α on the normalized maximum SIFs ($K_{\mathrm{I},k\max}(\theta)/K^0_{\mathrm{I},\max}(\theta)$ and $K_{\mathrm{II},k\max}(\theta)/K^0_{\mathrm{II},\max}(\theta)$) of each crack tip. For the Mode I SIFs of three non-parallel cracks (Fig. 2(a)), $K_{\mathrm{I},k\max}(\theta)/K^0_{\mathrm{I},\max}(\theta)$ values of tips A_1 and A_3 are equal to 1.01 and $K_{\mathrm{I},k\max}(\theta)/K^0_{\mathrm{I},\max}(\theta)$ of A_2 is 1.07 when α=0°, indicating that it is almost non-interaction. As α increases, $K_{\mathrm{I},k\max}(\theta)/K^0_{\mathrm{I},\max}(\theta)$ values of A_1 and A_2

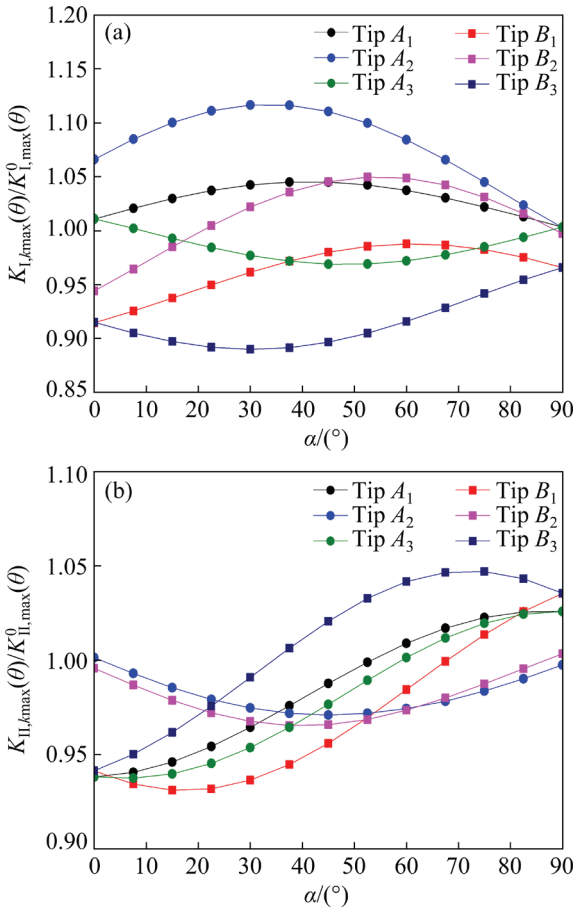

Fig. 2 Effects of relative inclination angle α on SIFs of all crack-tips: (a) $K_{\mathrm{I},k\max}(\theta)/K^0_{\mathrm{I},\max}(\theta)$; (b) $K_{\mathrm{II},k\max}(\theta)/K^0_{\mathrm{II},\max}(\theta)$

are always greater than 1. They first increase when $0 < \alpha \leq 30°$ (i.e., strengthening-interaction is strengthened) and then decrease when $30° < \alpha \leq 90°$ (i.e., strengthening-interaction is weakened). As $K_{\mathrm{I},k\max}(\theta)/K^0_{\mathrm{I},\max}(\theta)$ of A_3 is always smaller than 1, it is first decreased when $0 < \alpha \leq 45°$ (i.e., weakening-interaction is strengthened) and then increased when $45° < \alpha \leq 90°$ (i.e., weakening-interaction is weakened). Differently, $K_{\mathrm{I},k\max}(\theta)/K^0_{\mathrm{I},\max}(\theta)$ values of B_1 and B_3 are both smaller than 1 when $0 \leq \alpha \leq 90°$, meaning the weakening-interaction, while $K_{\mathrm{I},k\max}(\theta)/K^0_{\mathrm{I},\max}(\theta)$ of B_2 is less than 1 when $0 \leq \alpha \leq 25°$ and greater than 1 when $25° < \alpha \leq 90°$. In addition, for the Mode II SIFs (Fig. 2(b)), the values of $K_{\mathrm{II},k\max}(\theta)/K^0_{\mathrm{II},\max}(\theta)$ of A_1 and B_1, A_2 and B_2, and A_3 and B_3 are little changed (within 0.95−1.05) when $0 \leq \alpha \leq 90°$, indicating that the inclination angle α of the crack A_2B_2 has minor influence on the shear stress field. $K_{\mathrm{II},k\max}(\theta)/K^0_{\mathrm{II},\max}(\theta)$ values of A_2 and B_2 are always less than 1, and $K_{\mathrm{II},k\max}(\theta)/K^0_{\mathrm{II},\max}(\theta)$ values of A_1 and B_1, and A_3 and B_3 are changed from a value of less than 1 to a value of greater than 1, indicating that the multi-crack interaction changed from weakening to strengthening effect.

In summary, the strengthening zones of Mode I SIFs are α=7.5°−82.5° for the lower crack (A_1B_1), α=22.5°−82.5° for the middle crack (A_2B_2), and α=37.5°−82.5° for the upper crack (A_3B_3). The strengthening zones of Mode II SIFs are α=60°−90° for the lower crack (A_1B_1) and α=67.5°−90° for the upper crack (A_3B_3). There is no strengthening zone for the middle crack (A_2B_2). $K_{\mathrm{I},k\max}(\theta)/K^0_{\mathrm{I},\max}(\theta)$ value of A_2 is the maximum and $K_{\mathrm{I},k\max}(\theta)/K^0_{\mathrm{I},\max}(\theta)$ of B_3 is the minimum when α=30°. $K_{\mathrm{I},k\max}(\theta)/K^0_{\mathrm{I},\max}(\theta)$ value of A_1 is the maximum and $K_{\mathrm{I},k\max}(\theta)/K^0_{\mathrm{I},\max}(\theta)$ of A_3 is the minimum when α is 45°. $K_{\mathrm{I},k\max}(\theta)/K^0_{\mathrm{I},\max}(\theta)$ value of B_1 and B_2 is the largest when α is 60°. All cracks are in the strengthening zone when α is 45°.

(2) Variation of γ

Let D_s=D_s=0, D_h=20 mm, D_h=40 mm, β=45°, α=0°, a=15 mm, with only a change of γ. Figure 3 indicates the influence of γ on the normalized maximum SIFs $K_{\mathrm{I},k\max}(\theta)/K^0_{\mathrm{I},\max}(\theta)$ and $K_{\mathrm{II},k\max}(\theta)/K^0_{\mathrm{II},\max}(\theta)$ of each crack tip.

For the Mode I SIFs of three non-parallel cracks (Fig. 3(a)), $K_{\mathrm{I},k\max}(\theta)/K^0_{\mathrm{I},\max}(\theta)$ values of tips A_1 and A_3 are equal to 1.01 and $K_{\mathrm{I},k\max}(\theta)/K^0_{\mathrm{I},\max}(\theta)$ of A_2 is 1.07 when γ=0°, indicating that it is almost non-interaction. As γ increases, $K_{\mathrm{I},k\max}(\theta)/K^0_{\mathrm{I},\max}(\theta)$

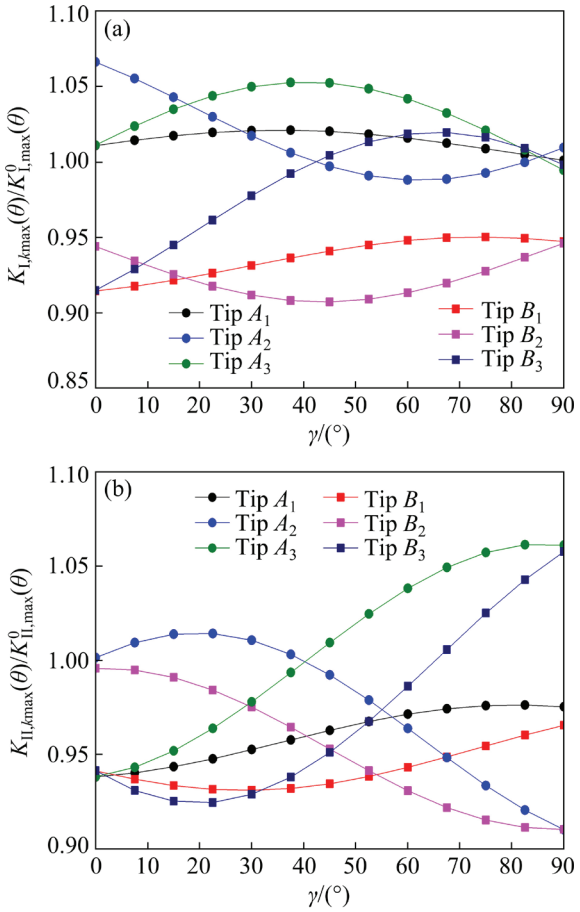

Fig. 3 Effects of relative inclination angle γ on SIFs of all crack-tips: (a) $K_{\mathrm{I},k\max}(\theta)/K^0_{\mathrm{I},\max}(\theta)$; (b) $K_{\mathrm{II},k\max}(\theta)/K^0_{\mathrm{II},\max}(\theta)$

values of A_1 and A_3 are always larger than 1. They first increase when $0 < \gamma \leq 37.5°$ (i.e., strengthening-interaction is strengthened) and then decrease when $37.5° < \gamma \leq 90°$ (i.e., strengthening-interaction is weakened). $K_{\mathrm{I},k\max}(\theta)/K^0_{\mathrm{I},\max}(\theta)$ of A_3 changes from a value of larger than 1 to a value of less than 1, and it first decreases when $0 < \gamma \leq 60°$ and then increases when $60° < \gamma \leq 90°$ (i.e., weakening-interaction is weakened). In contrast, $K_{\mathrm{I},k\max}(\theta)/K^0_{\mathrm{I},\max}(\theta)$ values of B_1 and B_2 are both less than 1 when $0 \leq \gamma \leq 90°$, meaning the weakening-interaction, while $K_{\mathrm{I},k\max}(\theta)/K^0_{\mathrm{I},\max}(\theta)$ of B_3 is less than 1 when $0 \leq \gamma \leq 57.5°$ and larger than 1 when $57.5° < \gamma \leq 90°$. In addition, for the Mode II SIFs (Fig. 3(b)), the values of $K_{\mathrm{II},k\max}(\theta)/K^0_{\mathrm{II},\max}(\theta)$ of A_1 and B_1, A_2 and B_2, and A_3 and B_3 change little (within 0.9−1.05) when $0 \leq \gamma \leq 90°$, indicating that the inclination angle γ has little influence on the shear stress field. $K_{\mathrm{II},k\max}(\theta)/K^0_{\mathrm{II},\max}(\theta)$ values of A_1 and B_1 are always smaller than 1 and $K_{\mathrm{II},k\max}(\theta)/$

$K^0_{II,max}(\theta)$ values of A_2 and B_2 change from a value of 1 to a value of less than 1. $K_{II,kmax}(\theta)/K^0_{II,max}(\theta)$ values of A_3 and B_3 change from a value of less than 1 to a value of greater than 1, indicating that the multiple crack interaction changes from a weakening effect to a strengthening effect.

In short, when γ changes, the strengthening zones of Mode I SIFs are γ=7.5°−75° for the lower crack (A_1B_1), γ=0°−37.5° for the middle crack (A_2B_2), and γ=7.5°−75° for the upper crack (A_3B_3). The strengthening zones of Mode II SIFs are γ=0°−45° for the middle crack (A_2B_2) and γ=37.5°−90° for the upper crack (A_3B_3). There is no strengthening zone for the lower crack (A_1B_1). $K_{I,kmax}(\theta)/K^0_{I,max}(\theta)$ values of A_1 and A_2 are the largest while that of B_2 is the smallest when γ is 45°. $K_{I,kmax}(\theta)/K^0_{I,max}(\theta)$ values of B_1 and B_3 are the largest and $K_{I,kmax}(\theta)/K^0_{I,max}(\theta)$ of A_2 is the smallest when γ is 75°. All cracks are located in the strengthening zone when γ is 45°. To avoid the possible failure of the strengthened zone of SIF, the relative inclination angle should not be 45°.

3 Experimental analysis of multiple crack initiation and propagation

3.1 Test arrangement

The uniaxial compression test of cracked rock specimens with the help of the strain gauge measurement method was adopted to study multiple cracks initiation and propagation. The rock material is red sandstone, selected from the Chuxiong City of Yunnan Province in China. Its basic mechanical parameters were tested by the International Society of Rock Mechanics (ISRM) standard test method (Table 1). Square cracked specimens of 100 mm × 100 mm × 20 mm were prepared (Fig. 4(a)), in which the relative positions of three cracks are the same as that in Section 2.2. Two groups of three-crack relative position parameters were selected for predicting initiation (Table 2). In the first group, D_s(D_s=0), $D_{s'}$($D_{s'}$=0), D_h(D_h=15 mm), and $D_{h'}$($D_{h'}$=30 mm), β=45°, and γ=0° were unchanged and α=15°−90°. In the second group, D_s(D_s=0), $D_{s'}$($D_{s'}$=0), D_h(D_h=15 mm), $D_{h'}$($D_{h'}$=30 mm), β=45°, and α=0° were unchanged and γ=15°−90°. Several 6.9 mm × 3.9 mm strain gauges (with a resistance of 120 Ω and sensitivity of 2.0 mV/V) were pasted on both sides above and below each crack of each specimen (Fig. 4(b)) because of uncertain crack-tip initiation position and direction before the test. The IMC multi-channel dynamic data acquisition system (made in Germany) was used to measure the resistance for strain calculation, including computer, data acquisition instrument (with 12 channels) and supporting software IMC Kansas.

The uniaxial compression test was conducted by the DNS100 electrohydraulic servo universal testing machine (with the maximum load of 1000 kN) under displacement control at the loading rate of 0.1 mm/s (Fig. 5). Before the tests, all specimens were wrapped with plastic film to obtain

Table 1 Basic mechanical parameters of red sandstone

σ_t/ MPa	σ_c/ MPa	φ/ (°)	E/ GPa	K_{IC}/ (MPa·m$^{1/2}$)	K_{IIC}/ (MPa·m$^{1/2}$)
3.75	65	33.5	9.08	0.47	1.22

σ_t is the tensile strength; σ_c is the compressive strength; φ is the internal frictional angle; E is the elastic modulus; K_{IC} is the Mode I fracture toughness; K_{IIC} is the Mode II fracture toughness

Table 2 Relative positions of rock specimen with three equal-length non-parallel cracks

Group	Specimen No.	α/(°)	γ/(°)
1	α1	15	0
	α2	30	0
	α3	45	0
	α4	60	0
	α5	75	0
	α6	90	0
2	γ1	0	15
	γ2	0	30
	γ3	0	45
	γ4	0	60
	γ5	0	75
	γ6	0	90

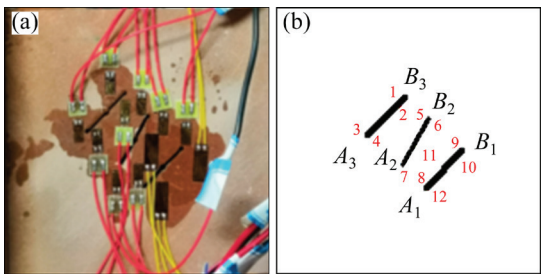

Fig. 4 Red sandstone specimen with strain gauges (α1): (a) Specimen; (b) Location of strain gauges

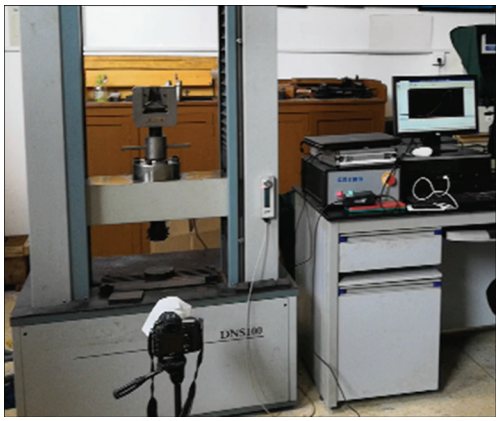

Fig. 5 Uniaxial compression test equipment of rock with three non-parallel cracks

the fracture trajectories. The stress−strain curves were automatically recorded by the machine during the test and the fracture trajectories of the rock specimens were photographed by a digital camera after the test.

3.2 Test results and analyses

(1) Strain−time curve and load−time curve (multiple cracks initiation sequence)

Figures 6 and 7 show the strain−time curves near the crack tips (obtained from different strain gauge channels) and load−time curve for the specimen $\alpha 1$, respectively. The crack point and time can be determined by the abrupt change point in the strain−time curves. The moments and directions corresponding to the strain gauges with the earliest mutations are taken as the crack tip initiation time.

For the specimen $\alpha 1$ (Fig. 6), the strain signals of strain gauges 7 and 8 first suddenly change at t=137 s and thus the crack tip A_2 was initiated first. And then the strain of strain gauge 7 was gradually decreased to be stable. The strain signal of the strain gauges 3 and 4 gradually increased from t=50 s and then largely increased to infinity at t=149 s, indicating the initiation of crack tip A_3 at t=149 s. The strain infinity is due to the tearing failure of the two strain gages caused by the crack propagation. It is not difficult to find that both the strain gauges 3 and 4 increased at the same time, but the increase rate of strain gauge 4 is always less than that of strain gauge 3. This is because the crack A_3B_3 mainly initiated in the direction of strain gauge 3, and the strain of strain gauge 3 is greater than that of strain gauge 4. The strain signals of strain gauges 11 and 12 were mutated simultaneously at t=156 s, thus the crack tips B_2 and A_1 were initiated

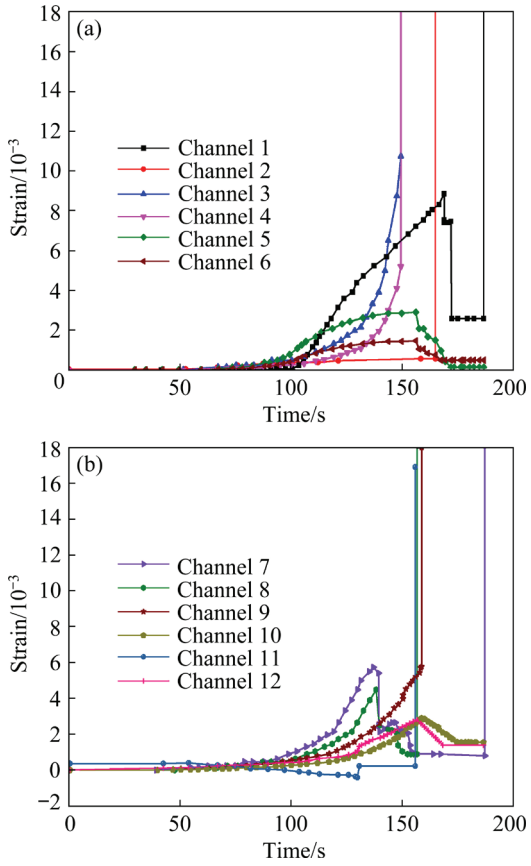

Fig. 6 Strain−time curves near crack tips of specimen $\alpha 1$ obtained by different channels: (a) Channels 1−6; (b) Channels 7−12

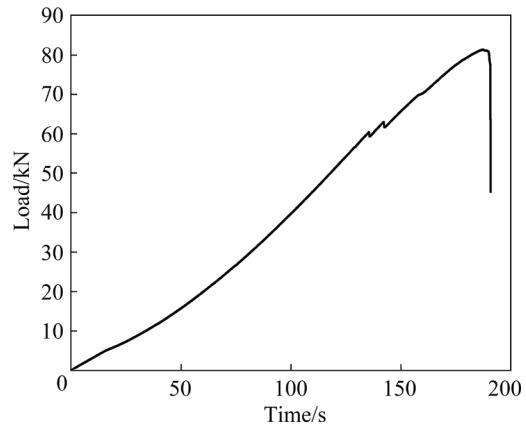

Fig. 7 Load−time curve for specimen $\alpha 1$

successively at t=156 s. The strain of strain gauge 11 tended to infinity due to failure of tensile tearing. The strain of strain gauge 12 gradually decreased until it became stable at t >170 s. The strain signals of strain gauges 5 and 6 reached the maximum at t=158 s and then slowly decreased, indicating the crack tip B_1 was initiated at t=158 s. The strain signals of strain gauges 9 and 10 started to increase slowly from t > 40 s, strain gauge 9 suddenly

increased to infinity at t=158 s and strain gauge 10 slowly decreased until it tended to be stable. Thus, the crack tip B_3 was initiated at t=165 s. The strain signal of strain gauge 2 was mutated to infinity at t=165 s. Figure 7 shows that the peak load reached the maximum at t=187 s. The huge amount of energy generated during the failure of the specimen causes the tearing failure of strain gauge 1.

Table 3 lists the crack initiation time (t) and initiation load (P^{ini}) at the crack tip for each specimen. It shows that the initial crack initiation time of each specimen first decreases and then increases with the increase of the crack relative inclination angle. The initial crack initiation time is the earliest and the crack initiation load is the smallest for α=45° or γ=45°. Each crack tip is rarely initiated at the same time, but rather in sequence with the loading time. The crack initiation tip and initiation time are different for each specimen. This indicates that the change of relative crack position has some influence on the crack initiation point, crack initiation sequence, and crack initiation time. Most of the cracks were initiated first at A_2 or B_2 tip (the center tip of the specimen), and the last cracks were initiated at B_1 or B_3 tip (the tip closest to the specimen boundary). The later the crack initiation time is, the closer the initiation load is to the peak load. The failure of the specimen usually occurs a few seconds after the initiation of the last tip, rather than immediately.

(2) Stress−strain curve (multiple cracks initiation stress and ultimate stress)

The stress−strain curves of red sandstone specimens with three non-parallel cracks of different relative positions are all divided into four stages under uniaxial compression (Fig. 8): initial compaction stage, linear elastic deformation stage,

Table 3 Crack initiation parameters of each specimen

Specimen No.	Parameter	Crack tip (Channel No.)						Crack initiation order
		A_1 (11,12)	B_1 (9,10)	A_2 (7,8)	B_2 (5,6)	A_3 (3,4)	B_3 (1,2)	
α1	t/s	157	158	137	156	149	165	$A_2\rightarrow A_3\rightarrow B_2\rightarrow A_1\rightarrow B_1\rightarrow B_3$
	P^{ini}/kN	69.22	69.93	60.4	68.84	65.24	72.71	
α2	t/s	120	123	158	160	144	156	$A_1\rightarrow B_1\rightarrow A_3\rightarrow B_3\rightarrow A_2\rightarrow B_2$
	P^{ini}/kN	59.64	56.84	78.32	78.08	70.21	77.49	
α3	t/s	97	224	96	132	136	133	$A_2\rightarrow A_1\rightarrow B_2\rightarrow B_3\rightarrow A_3\rightarrow B_1$
	P^{ini}/kN	50.69	80.85	51.5	72.95	75.39	73.36	
α4	t/s	135	142	130	137	140	139	$A_2\rightarrow A_1\rightarrow B_2\rightarrow B_3\rightarrow A_3\rightarrow B_1$
	P^{ini}/kN	69.87	73.98	69.47	71.15	72.88	72.38	
α5	t/s	152	154	110	149	112	155	$A_2\rightarrow A_3\rightarrow B_2\rightarrow A_1\rightarrow B_1\rightarrow B_3$
	P^{ini}/kN	69.44	70.56	43.75	67.49	45.2	70.96	
α6	t/s	150	148	138	152	134	153	$A_3\rightarrow A_2\rightarrow B_1\rightarrow A_1\rightarrow B_2\rightarrow B_3$
	P^{ini}/kN	85.94	85	83.02	86.41	83	86.67	
γ1	t/s	163	166	130	155	148	132	$A_2\rightarrow B_3\rightarrow A_3\rightarrow B_2\rightarrow A_1\rightarrow B_1$
	P^{ini}/kN	78.03	78.98	65.82	74.39	73.42	62.39	
γ2	t/s	142	147	157	169	133	131	$B_3\rightarrow A_3\rightarrow A_1\rightarrow B_1\rightarrow A_2\rightarrow B_2$
	P^{ini}/kN	67.09	70.75	73.76	81.6	63.83	64.65	
γ3	t/s	151	162	97	165	96	157	$A_3\rightarrow A_2\rightarrow A_1\rightarrow B_3\rightarrow B_1\rightarrow B_2$
	P^{ini}/kN	84.8	86.91	48.75	87.79	48.72	84.93	
γ4	t/s	146	163	117	148	119	161	$A_2\rightarrow A_3\rightarrow A_1\rightarrow B_2\rightarrow B_3\rightarrow B_1$
	P^{ini}/kN	70.59	82.04	53.86	72.08	53.35	80.78	
γ5	t/s	135	145	112	133	115	142	$A_2\rightarrow A_3\rightarrow B_2\rightarrow A_1\rightarrow B_3\rightarrow B_1$
	P^{ini}/kN	73.22	78.3	59.62	71.92	59.15	77.59	
γ6	t/s	142	148	146	150	100	130	$A_3\rightarrow B_3\rightarrow A_1\rightarrow A_2\rightarrow B_1\rightarrow B_2$
	P^{ini}/kN	79.69	82.1	81.75	83.04	57.07	81.7	

non-linear deformation stage and post-peak failure stage. Figure 9 shows the crack initiation stress and ultimate stress. It can be seen that the crack relative inclination angle (α or γ) has little effect on the elastic modulus (Fig. 8) but has a great effect on the crack initiation stress and ultimate stress (Fig. 9). The crack initiation stress first increases when α=γ=0°−15° and then decreases when α=γ=15°−45°. The crack initiation load reaches its maximum when α=90° or γ=15°. The ultimate stress first decreases when α=γ=0°−30° and increases when α=γ=30°−45°. The ultimate stress reaches the maximum when α=90° or γ=45°.

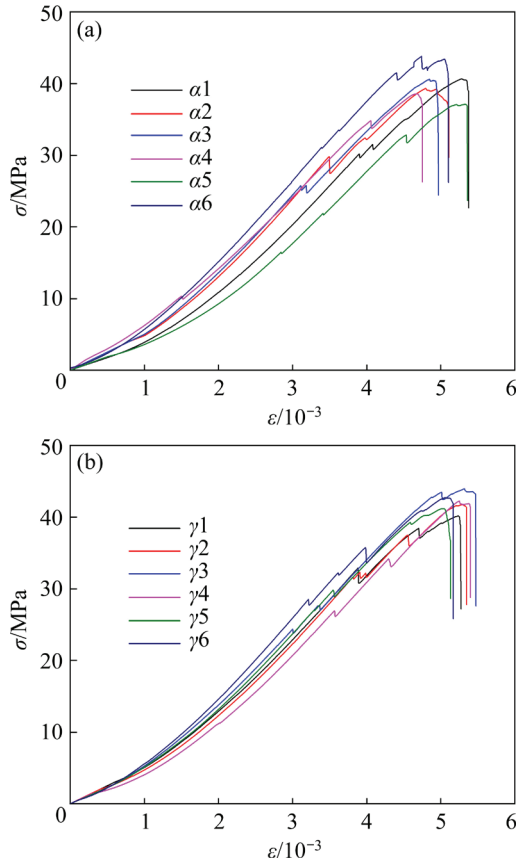

Fig. 8 Stress−strain curves of red sandstone specimens with three non-parallel cracks: (a) Variation of α; (b) Variation of γ

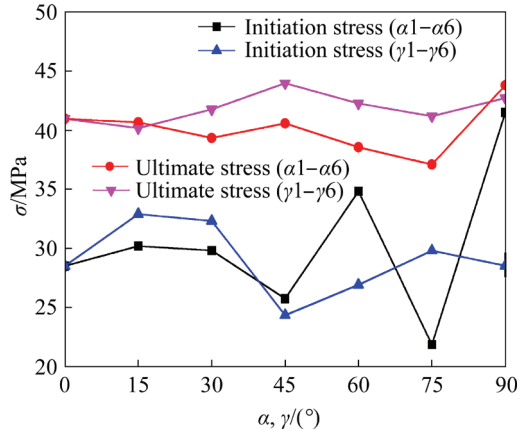

Fig. 9 Crack initiation stress and ultimate stress of red sandstone specimens with three non-parallel cracks

For red sandstone specimens with three equal-length non-parallel cracks under uniaxial compression, the variation law of crack initiation load is the same when α and γ are both less than 60°. Differently, the variation law of the crack initiation load is opposite when α and γ are both larger than 60°. It shows that the effect of the rotation of the middle crack (A_2B_2) and upper crack (A_3B_3) on the crack initiation load has a mutation at 60°. The change rule of ultimate stress is the same as the crack relative angle changes (whether α or γ changes). It indicates that the effect of rotation of the middle crack (A_2B_2) and the upper crack (A_3B_3) on the ultimate stress is the same. The deformation of the specimens in the post-peak failure stage is consistent, illustrating that different crack locations have little influence on the failure stage of the stress−strain curve.

(3) Fracture trajectory and mechanism analysis

Figure 10 shows the test propagation trajectory of red sandstone specimens with three equal-length non-parallel cracks under uniaxial compression. Table 4 lists the test results of three crack initiation parameters under uniaxial compression, including crack initiation load, crack initiation tip, crack initiation angle, and crack initiation mechanism. The fracture modes of red sandstone specimens with three non-parallel cracks under uniaxial compression can be roughly classified into two forms: wing crack penetration (α3, γ1, γ5) and wing crack−secondary crack penetration (α1, α2, α4, α5, α6, γ2, γ3, γ4, γ6).

Take α1 and α3 as examples to illustrate the crack propagation mechanism. For specimen α1, the crack tip A_2 was first initiated at a negative angle (θ < 0°) at t=137 s, and the wing crack stopped propagating after propagating a short distance. Then, the crack tip A_3 was initiated at a positive angle at t=149 s, and then steadily expanded towards the specimen boundary. The crack tip B_2 was initiated at a negative initiation angle and t=156 s, and the wing crack propagated in the direction of A_1, causing the crack initiation of A_1 at t=157 s. At this point, cracks A_2B_2 and A_1B_1 were joined in a "Z" shape. Crack tip B_1 was initiated at a positive crack

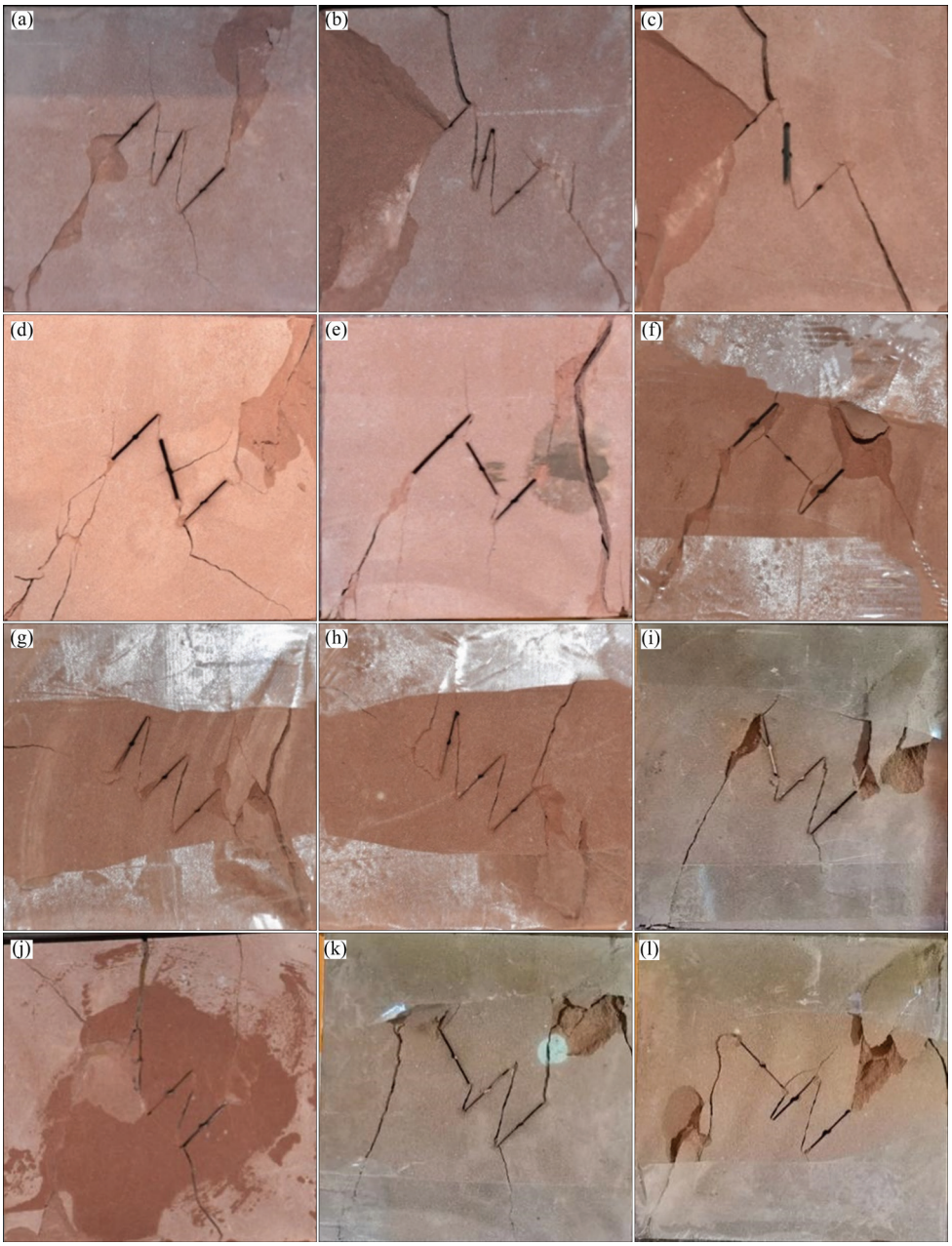

Fig. 10 Fracture trajectories of red sandstone specimen with three non-parallel cracks: (a) α1 (α=15°); (b) α2 (α=30°); (c) α3 (α=45°); (d) α4 (α=60°); (e) α5 (α=75°); (f) α6 (α=90°); (g) γ1 (γ=15°); (h) γ2 (γ=30°); (i) γ3 (γ=45°); (j) γ4 (γ=60°); (k) γ5 (γ=75°); (l) γ6 (γ=90°)

initiation angle and t=158 s, and the wing crack expanded steadily along the specimen boundary, accompanied by the appearance of secondary cracks. Finally, the crack tip B_3 initiated at a negative angle and t=165 s, and the wing crack propagated along the direction of A_2 and connected with it ("*Z*" shape). Secondary cracks in the opposite direction appeared after the initiation of B_3 and the secondary cracks propagated towards the specimen boundary except wing cracks. The failure area of specimen α1 was mainly concentrated around the crack and the three main cracks were connected in the form of a tension−shear composite mode with a "sawtooth". The failure of the specimen is due to the interaction between the primary crack and the secondary cracks. The initiation mechanism of all crack tips is Mode I. Therefore, the failure mode of the specimen α1 can be defined as wing crack−secondary crack penetration.

For specimen α3, the crack tip A_2 was initiated at a positive crack initiation angle ($\theta > 0°$) (crack

Table 4 Test results of crack initiation parameters for all specimens

Group No.	Specimen No.	Initiation load/MPa	Initiation tip	Initiation angle/(°)	Initiation mode
1	α1	30.2	A_2	−144	Mode I
	α2	29.82	A_1	−119	Mode I
	α3	25.75	A_2	25	Mode I
	α4	34.735	A_2	−26	Mode I
	α5	21.875	A_2	−47	Mode I
	α6	41.5	A_3	39	Mode I
2	γ1	32.91	A_2	−124	Mode I
	γ2	32.325	B_3	−166	Mode I
	γ3	24.36	A_3	17	Mode I
	γ4	26.93	A_2	−127	Mode I
	γ5	29.81	A_2	−123	Mode I
	γ6	28.535	A_3	59	Mode I

initiation load is 51.5 kN) at t=97 s, and the wing crack propagated along the direction of A_1 and penetrated with it. The crack tip B_2 was initiated at the negative angle and t=132 s, and the wing crack propagated toward the direction of B_3, causing the initiation of crack tip B_3. The wing crack generated by B_3 propagated to the specimen boundary. Then, crack tip A_3 was initiated at the positive angle and t=136 s, and the wing crack slowly propagated towards the specimen boundary. Finally, the crack tip B_1 was initiated at the negative angle and t=224 s, and the wing crack propagated towards the specimen boundary. The failure of specimen α3 is the result of the crack propagation of the two main wings, and all of the crack initiation mechanisms are Mode I. Therefore, the failure mode of the specimen α3 can be defined as wing crack−wing crack penetration.

In conclusion, the main crack initiation process is always accompanied by the appearance of secondary cracks, and the failure trajectory is generally "Z" shaped, zig-zag. All crack tips are Mode I (tensile) initiation. For some specimens (such as α2 and α3, γ1, γ2, and γ4), the crack initiation load of the first crack initiation tip is greater than that of the second crack initiation tip. This is because the stress−strain curve appears as a short descending section after the first crack tip is initiated, and the second crack initiation point is located at the descending section.

4 Initiation mechanism analysis of non-parallel multiple cracks

4.1 Initiation criterion of multiple cracks

According to the criterion of maximum tension-to-shear SIF ratio [26], the non-parallel multiple cracks initiation criterion can be established as follows:

$$\begin{cases} \dfrac{K_{\mathrm{I},k}(\theta_k)_{\max}}{K_{\mathrm{II},k}(\theta_k)_{\max}} > \dfrac{K_{\mathrm{IC}}}{K_{\mathrm{IIC}}}, K_{\mathrm{I},k}(\theta_k)_{\max} = K_{\mathrm{IC}} \\ \quad \text{at } \theta_{\mathrm{IC},k}, \text{ Mode I fracture} \\ \dfrac{K_{\mathrm{I},k}(\theta_k)_{\max}}{K_{\mathrm{II},k}(\theta_k)_{\max}} < \dfrac{K_{\mathrm{IC}}}{K_{\mathrm{IIC}}}, K_{\mathrm{II},k}(\theta_k)_{\max} = K_{\mathrm{IIC}} \\ \quad \text{at } \theta_{\mathrm{IIC},k}, \text{ Mode II fracture} \end{cases} \tag{4}$$

4.2 Initiation parameter and mechanism prediction of three non-parallel cracks

Take the same red sandstone as rock material (Table 1) to predict the initiation process of three non-parallel cracks in the infinite plate under uniaxial compression. The relative positions of the three non-parallel cracks are the same as those in Table 2. The calculation process for predicting the initiation parameters of three non-parallel cracks is the same as that for the three parallel cracks in Ref. [26].

Table 5 lists the prediction results of the

Table 5 Prediction results of crack initiation parameters for all specimens

Group No.	Specimen No.	Initiation stress/MPa	Initiation tip	Initiation angle/(°)	Initiation mode
1	α1	29.34	A_2	−125.48	Mode I
	α2	29.29	A_1	−126.27	Mode I
	α3	28.92	A_2	50.84	Mode I
	α4	28.45	A_2	−50.54	Mode I
	α5	28.99	A_2	−53.53	Mode I
	α6	29.07	A_3	52.68	Mode I
2	γ1	29.91	A_2	−129.90	Mode I
	γ2	28.57	B_3	−125.51	Mode I
	γ3	28.42	A_3	52.86	Mode I
	γ4	28.70	A_2	−127.42	Mode I
	γ5	29.15	A_2	−129.4	Mode I
	γ6	28.95	A_3	55.37	Mode I

initiation of three non-parallel cracks. It can be seen that the crack initiation stress decreases with the increase of the relative inclination angle when γ is less than 45°. The crack initiation stress first increases and then decreases with the increase of the relative inclination angle when γ is in the range of 45°−90°. It is not difficult to find that the change of γ has the same effect on the positive or negative value of the crack initiation angle. The crack initiation load of all specimens changes little (less than 2 MPa) because the crack distributions (relative inclination angles) of the two groups are all in the possible danger zone and have almost no influence on the crack initiation load. All crack tips are Mode I (tensile) initiation.

4.3 Comparison between theoretical and experimental results

Figure 11 shows the comparison between the test propagation trajectory (black line) and the predicted propagation trajectory (red line). It can be found that the crack initiation angles of most

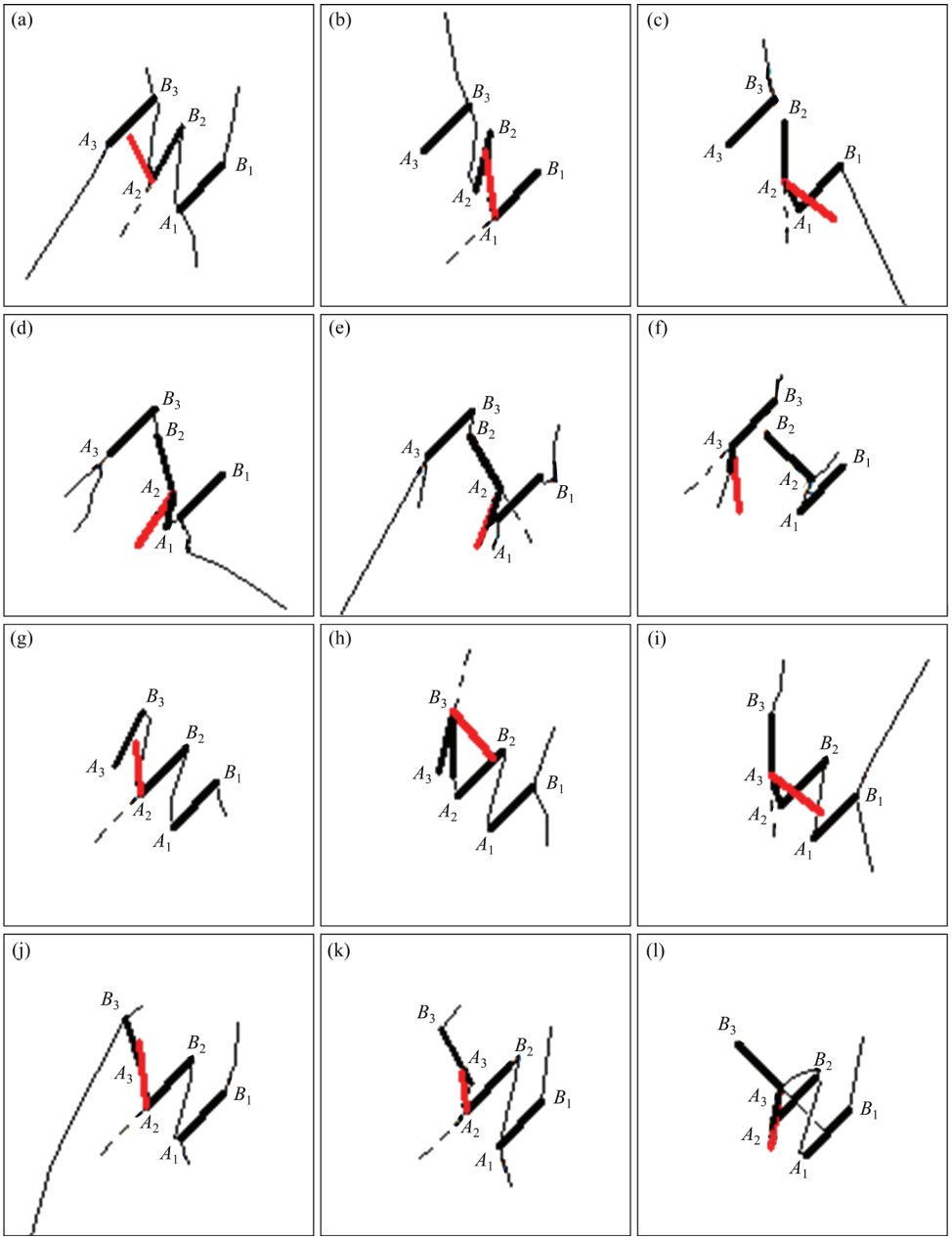

Fig. 11 Comparison between test and predicted fracture trajectories of red sandstone specimens with three non-parallel cracks (red line: predicted trajectory; black line: test trajectory): (a) $\alpha 1$ (α=15°); (b) $\alpha 2$ (α=30°); (c) $\alpha 3$ (α=45°); (d) $\alpha 4$ (α=60°); (e) $\alpha 5$ (α=75°); (f) $\alpha 6$ (α=90°); (g) $\gamma 1$ (γ=15°); (h) $\gamma 2$ (γ=30°); (i) $\gamma 3$ (γ=45°); (j) $\gamma 4$ (γ=60°); (k) $\gamma 5$ (γ=75°); (l) $\gamma 6$ (γ=90°)

specimens are in good agreement and verify the validity of the theoretical results. The fracture trajectories of the individual specimens (such as $\gamma 2$) appear some variation. Table 4 and Table 5 show that the crack initiation load and crack initiation tip of most test results agree with the predicted results, which validates the availability of the multiple crack propagation theory. The slight differences in fracture trajectory are due to the heterogeneity and anisotropy of the natural rock materials, which are assumed to be isotropic, homogeneous, and continuous in the theoretical calculation.

5 Conclusions

(1) $K_{\mathrm{I},k\max}(\theta)$ and $K_{\mathrm{II},k\max}(\theta)$ of the three non-parallel oblique cracks varying with the relative inclination angle are calculated to reveal the interaction mechanism of multiple cracks and determine the strengthening and weakening zones of SIF. The multiple crack initiation criterion based on the ratio of maximum tensile-to-shear SIF is used to predict the initiation of non-parallel multiple cracks.

(2) To avoid the possible failure of the strengthened zone of stress intensity factor, the relative inclination angle should not be times of 15°. The prediction results well agree with the test results, which validates the validity of the theoretical results. All of the fracture mechanisms are Mode I (tensile) initiation.

(3) Multiple crack tips are rarely initiated at the same time, but sequentially with the loading time. The middle crack tip is usually initiated at one tip first and the lower crack tip is initiated at one tip last. Failure of the specimen usually occurs a few seconds after the initiation of the last tip, rather than immediately.

(4) For red sandstone specimens with three equal-length non-parallel cracks under uniaxial compression, the variation law of crack initiation load is the same when α and γ are both less than 60°. The variation law of crack initiation load is the opposite when α and γ are both larger than 60°. The peak load change law is the same when the crack relative angle changes (whether α or γ changes).

(5) For the red sandstone specimens with three arbitrary cracks under uniaxial compression, there are two different failure modes: the failure of the specimen is due to the interaction between the main crack and the secondary crack (wing crack−secondary crack coalescence); the failure of the specimen is due to the crack propagation of two main wings (wing crack coalescence). The failure trajectory is generally "*Z*" shaped, zig-zagging.

CRediT authorship contribution statement

Qing-qing SHEN: Methodology, Investigation, Software, Visualization, Writing − Original draft, Writing − Review & editing; **Dian-yi HUANG:** Resources, Validation, Writing − Review & editing; **Qiu-hua RAO:** Methodology, Conceptualization, Funding acquisition, Project administration, Supervision. **Wei YI:** Validation; **Dong-liang SUN:** Validation; **Zhuo LI**: Validation.

Declaration of competing interest

The authors declare that they have no known competing financial interests or personal relationships that could have appeared to influence the work reported in this paper.

Acknowledgments

This work was supported by the National Natural Science Foundation of China (Nos. 51874351, 52078495), and Hunan Institute of Technology Introduced Talents Research Start-up Fund Project, China (No. HQ22016).

References

[1] SHEN Bao-tang. The mechanism of fracture coalescence in compression—Experimental study and numerical simulation [J]. Engineering Fracture Mechanics, 1995, 51(1): 73−85.

[2] JIANG Tong, PAN Xu-wei, LEI Jia-hua, ZHANG Jun-ran, WANG Wen-xue. Rupture and crack propagation in artificial soft rock with preexisting fractures under uniaxial compression [J]. Geotechnical and Geological Engineering, 2019, 37(3): 1943−1956.

[3] GUO Jia-qi, LIU Peng-fei, HUANG Shan-xiu, QIAN Yuan, LIU Guang-jun. Cracking processes and failure modes of rock-like specimens with a set of non-persistent joints [J]. Geotechnical and Geological Engineering, 2021, 39(2): 1237−1257.

[4] PARK C H, BOBET A. Crack initiation, propagation and coalescence from frictional flaws in uniaxial compression [J]. Engineering Fracture Mechanics, 2010, 77(14): 2727−2748.

[5] LEE H, JEON S. An experimental and numerical study of fracture coalescence in pre-cracked specimens under uniaxial compression [J]. International Journal of Solids and Structures, 2011, 48(6): 979−999.

[6] YANG Sheng-qi, LIU Xiang-ru, JING Hong-wen. Experimental investigation on fracture coalescence behavior of red sandstone containing two unparallel fissures under uniaxial compression [J]. International Journal of Rock Mechanics and Mining Sciences, 2013, 63: 82−92.

[7] YANG Ren-shu, CHEN Cheng, WANG Xu, ZUO Jin-jing, FANG Shi-zheng, MEI Bi. Experimental investigation on the influence of different diameter empty holes on the crack growth behavior of blasting [J]. Journal of China Coal Society, 2017, 42(10): 2498−2503. (in Chinese)

[8] ZHANG Jian-zhi, ZHOU Xiao-ping, ZHOU Lun-shi, BERTO F. Progressive failure of brittle rocks with non-isometric flaws: Insights from acousto−optic−mechanical (AOM) data [J]. Fatigue & Fracture of Engineering Materials & Structures, 2019, 42(8): 1787−1802.

[9] ZHOU Xiao-ping, ZHANG Jian-zhi, BERTO F. Fracture analysis in brittle sandstone by digital imaging and AE techniques: Role of flaw length ratio [J]. Journal of Materials in Civil Engineering, 2020, 32(5): 04020085.

[10] ZHOU Xiao-ping, WANG Yun-teng, ZHANG Jian-zhi, LIU Fei-nan. Fracturing behavior study of three-flawed specimens by uniaxial compression and 3D digital image correlation: Sensitivity to brittleness [J]. Rock Mechanics and Rock Engineering, 2019, 52(3): 691−718.

[11] ZHOU Xiao-ping, ZHANG Jian-zhi, YANG Sheng-qi, BERTO F. Compression-induced crack initiation and growth in flawed rocks: A review [J]. Fatigue & Fracture of Engineering Materials & Structures, 2021, 44(7): 1681−1707.

[12] CHAKRABORTY D, MURTHY K S R K, CHAKRABORTY D. Determination of K_I in orthotropic laminates with double ended cracks using a single strain gage technique [J]. Theoretical and Applied Fracture Mechanics, 2016, 82: 96−106.

[13] CHAKRABORTY D, CHAKRABORTY D, MURTHY K S R K. A strain gage technique for the determination of mixed mode stress intensity factors of orthotropic materials [J]. Composite Structures, 2017, 160: 185−194.

[14] SARANGI H, MURTHY K S R K, CHAKRABORTY D. Optimum strain gage location for evaluating stress intensity factors in single and double ended cracked configurations [J]. Engineering Fracture Mechanics, 2010, 77(16): 3190−3203.

[15] SARANGI H, MURTHY K S R K, CHAKRABORTY D. Radial locations of strain gages for accurate measurement of mode I stress intensity factor[J]. Materials & Design, 2010, 31(6): 2840−2850.

[16] SARANGI H, MURTHY K S R K, CHAKRABORTY D. Experimental verification of optimal strain gage locations for the accurate determination of mode I stress intensity factors [J]. Engineering Fracture Mechanics, 2013, 110: 189−200.

[17] LI Xiao-zhao, QI Cheng-zhi, SHAO Zhu-shan, MA Chao. Evaluation of strength and failure of brittle rock containing initial cracks under lithospheric conditions [J]. Acta Geophysica, 2018, 66(2): 141−152.

[18] HASEBE N, WANG X F, KONDO M. Interaction between crack and arbitrarily shaped hole with stress and displacement boundaries [J]. International Journal of Fracture, 2003, 119(1): 83−102.

[19] ZHANG Xing. Fracture and damage mechanics [M]. Beijing: Beijing University of Aeronautics & Astronautics Press, 2009: 125−130. (in Chinese)

[20] WANG X, LAMBERT S B. Weight functions and stress intensity factors for semi-elliptical cracks in T-plate welded joints [J]. Fatigue and Fracture of Engineering Materials and Structures, 1998, 21(1): 99−117.

[21] WESTERGAARD H M. Bearing pressures and cracks [J]. Journal of Applied Mechanics, 1939, 61: 49−53.

[22] KEER L M, NEMAT-NASSER S, ORANRATNACHAI A. Spontaneous growth of interacting cracks in a cruciform pattern [J]. Engineering Fracture Mechanics, 1980, 13(1): 15−29.

[23] WILLIAMS M L. On the stress distribution at the base of a stationary crack [J]. Journal of Applied Mechanics, 1957, 24(1): 109−114.

[24] KACHANOV M. Elastic solids with many cracks: A simple method of analysis [J]. International Journal of Solids and Structures, 1987, 23(1): 23−43.

[25] CHEN Yi-zhou. General case of multiple crack problems in an infinite plate [J]. Engineering Fracture Mechanics, 1984, 20(4): 591−597.

[26] SHEN Qing-qing, RAO Qiu-hua, LI Zhuo, YI Wei, SUN Dong-liang. Interacting mechanism and initiation prediction of multiple cracks [J]. Transactions of Nonferrous Metals Society of China, 2021, 31(3): 779−791.

[27] SHEN Qing-qing, RAO Qiu-hua, ZHANG Quan, LI Zhuo, SUN Dong-liang, YI Wei. A new method for predicting double-crack propagation trajectories of brittle rock [J]. International Journal of Applied Mechanics, 2021, 13(2): 1−21.

[28] ERDOGAN F, SIH G C. On the crack extension in plates under plane loading and transverse shear [J]. Journal of Basic Engineering, 1963, 85: 519−527.

[29] MAITI S K, SMITH R A. Comparison of the criteria for mixed mode brittle fracture based on the preinstability of stress-strain field [J]. International Journal of Fracture, 1984, 24(1): 5−22.

[30] CHANG K J. On the maximum strain criterion—A new approach to the angled crack problem [J]. Engineering Fracture Mechanics, 1981, 14(1): 107−124.

[31] PALANISWAMY K, KNAUSS W G. Propagation of a crack under general, in-plane tension [J]. International Journal of Fracture Mechanics, 1972, 8(1): 114−117.

[32] SIH G C. Strain−energy−density factor applied to mixed mode crack problems [J]. International Journal of Fracture, 1974, 10(3): 305−321.

[33] RAO Qiu-hua, SUN Zong-qi, STEPHANSSON O, LI Chun-lin, STILLBORG B. Shear fracture (Mode II) of brittle rock [J]. International Journal of Rock Mechanics and Mining Sciences, 2003, 40: 355−375.

[34] WANG Zhi. Plane shear (Mode II) and anti-plane shear (Mode III) fracture theory and experiment analysis of rock at high temperatures [D]. Changsha: Central South University,

2007. (in Chinese)

[35] LI Peng, RAO Qiu-hua, LI Zhuo, JING Jing. Thermal-hydro-mechanical coupling stress intensity factor of brittle rock [J]. Transactions of Nonferrous Metals Society of China, 2014, 24(2): 499−508.

[36] YI Wei, RAO Qiu-hua, LI Zhuo, SUN Dong-liang, SHEN Qing-qing. Thermo−hydro−mechanical−chemical (THMC) coupling fracture criterion of brittle rock [J]. Transactions of Nonferrous Metals Society of China, 2021, 31(9): 2823−2835.

基于应变片法的非平行多裂纹相互作用及起裂机理

沈晴晴[1,2]，黄典一[1]，饶秋华[1]，易 威[1]，孙栋良[1]，李 卓[1]

1. 中南大学 土木工程学院，长沙 410075；
2. 湖南工学院 土木与建筑工程学院，衡阳 421002

摘 要：通过计算 3 条非平行斜裂纹的最大应力强度因子 $K_{\mathrm{I},k\max}(\theta)$和 $K_{\mathrm{II},k\max}(\theta)$，揭示其相互作用机理，并采用多裂纹起裂准则预测非平行多裂纹的起裂参数。对含 3 条非平行斜裂纹的红砂岩试样开展单轴压缩试验，采用应变片测量方法监测裂纹尖端附近的应变，以确定裂纹起裂顺序。结果表明：裂缝相对倾角的变化对破坏轨迹影响不大且多裂纹尖端很少同时起裂。单轴压缩下含 3 条非平行斜裂纹红砂岩试件破坏形式可分为两种：翼裂纹贯通和翼裂纹−次生裂纹贯通。断裂机理均为 I 型(拉伸)起裂。预测结果与试验结果吻合较好，验证了理论结果的有效性。

关键词：非平行多裂纹；相互作用机理；起裂机理；应变片法

(Edited by Wei-ping CHEN)